In Situ Atomic Force Microscopy as a Tool for Investigating Interactions and Assembly Dynamics in Biomolecular and Biomineral Systems

James J. De Yoreo, Sungwook Chung, and Raymond W. Friddle*

Atomic force imaging and spectroscopy provide unique tools for investigating molecular interactions and dynamics in biomolecular and biomineral systems in situ. Herein, three recent examples of methods used to gain mechanistic insights into the self-assembly of protein matrices and biomolecular controls over mineral formation are reviewed. Studies of S-layer protein assembly reveal the complex nature of the nucleation and growth pathway, demonstrate the importance of kinetic traps in determining that pathway and provide quantification of the energy barriers controlling formation rates. Investigations of citrate and polypeptide modification of calcium oxalate monohydrate growth combined with molecular dynamics simulations (MD) demonstrate the importance of stereochemical matching at atomic steps on the crystal surface and establish a direct relationship between the step edge binding energies and shape modification. Measurements of step kinetics lead to detailed atomic-scale models that include both thermodynamic and kinetic effects, including time-dependent phenomena related to the multi-stage binding dynamics of polypeptide chains. Dynamic force spectroscopy measurements of binding between amelogenin peptide segments and hydroxyapatite (HAP) crystal faces, again combined with MD simulations, establish an energetic rationale for the observed c-axis elongation characteristic of HAP in tooth enamel, based on determinations of the peptide-HAP binding free energy. These examples demonstrate the deep level of understanding that can be obtained by applying in situ AFM imaging and force spectroscopy to biomolecular and biomineral systems.

1. Introduction

The formation of materials in biological and environmental systems, whether through assembly of protein complexes or biologically-directed mineral nucleation and growth, typically occurs in aqueous media. While this environment presents many challenges to both theoretical and experimental lines of investigation, it presents an opportunity for application of atomic force microscopy (AFM). Both imaging and dynamic force spectroscopy (DFS) can be carried out in fluids; consequently the interactions of proteins with other proteins or surfaces, protein aggregation and self-assembly, and mineral nucleation and growth can all be probed in situ with resolution at the level of single proteins and atomic step heights. This capability has a number of scientific impacts. First, the dynamics of these processes and, ultimately, the structure and morphology of the final state reflect the energy landscape seen by the constituent ions and molecules. DFS provides a means for directly probing the free energies of binding while measurements of assembly, nucleation, and growth rates indirectly probe kinetic and/or free energy barriers that determine the rates of these processes. Second, an in situ imaging capability removes the ambiguity associated with deducing pathways of formation by observation of a final structure or morphology. There are many technological challenges associated with applying in situ AFM imaging and DFS to protein and biomineral systems, but rarely are they insurmountable. Here we review some recent investigations by the authors of three phenomena: protein self-assembly, bio-organic modification of mineral growth, and protein-mineral surface interactions, and illustrate the unique information obtained through in situ AFM imaging and spectroscopy.

2. Protein Self-Assembly

Self-assembled protein architectures exhibit a range of structural motifs[1] including particles,[2] fibers,[3] ribbons,[4] and sheets.[5] Their functions include selective transport,[5] structural scaffolding,[6] mineral templating,[4,7] and propagation of or protection from pathogenesis.[3,8] Although the molecular structures of the isolated proteins dictate their governing interactions, these functions emerge from the nanoscale organization that arises out of self-assembly. Typically, proteins that naturally

---

Dr. J. J. De Yoreo[+]
The Molecular Foundry and
Materials Sciences Division
Lawrence Berkeley National Laboratory
One Cyclotron Road, Berkeley, CA 94720, USA
E-mail: james.deyoreo@pnnl.gov
Dr. S. Chung
The Molecular Foundry and Physical Biosciences Division
Lawrence Berkeley National Laboratory
One Cyclotron Road, Berkeley, CA 94720, USA
Dr. R. W. Friddle
Sandia National Laboratories
Livermore, CA 94550, USA
[+]Present address: Pacific Northwest National Laboratory
P.O. Box 999, MS K2-01
Richland, WA 99352, USA

DOI: 10.1002/adfm.201203424

self-assemble into extended ordered structures adopt conformations that are distinct from those of the individual monomeric proteins.[9–11] For example, collagen matrices, which constitute the organic scaffolds of bones and teeth in all higher organisms, are constructed from triple helices of the individual collagen monomers.[11] These helices further assemble into highly organized, twisted fibrils exhibiting a pseudo-hexagonal symmetry. In some cases, assembly is inexorably linked to folding transformations, as in the case of prion or amyloid fibrils, where mis-folding of the monomers triggers assembly, which in turn drives mis-folding of new monomers.[9] None-the-less, while the phenomenon of folding by individual proteins has been well explored both experimentally and theoretically, much less attention has been given to protein assembly.

Recently, in situ AFM was used to investigate the dynamics and underlying mechanisms of S-layer protein assembly.[12,13] S-layers are a class of proteins that assemble into 2D crystalline sheets forming the outermost membranes of many bacteria and Archaea.[14] The crystalline lattice is typically built from multimeric growth units of the individual S-layer monomers, which in some cases can adopt more than one structural conformation within a single membrane.[15] The individual proteins, which can have molecular weights of hundreds of kDa, are produced within the cell, but must be assembled on the outside. They typically overlie a lipid membrane or polymeric cell wall and exhibit crystal symmetries ranging from p1 to p6. They play a role in all the functions of self-assembled protein structures listed above and can be reconstituted in vitro into 2D arrays both in bulk solutions and at surfaces. Because they exhibit large-scale order and a periodicity commensurate with the dimensions of quantum dots and nanotubes, they were amongst the first self-assembled protein structures to be exploited as scaffolds for organizing nanostructures via a bottom-up approach.[16]

In order to gain insight into the assembly process, Chung et al.[12] used in situ AFM to follow the nucleation and growth of the S-layer SbpA from *Lysinibacillus sphaericus* (ATCC 4525, MW = 132 kDa) on supported lipid bilayers (SLB) of 1-palmitoyl-2-oleoyl-sn-glycero-3 phosphocholine (POPC) deposited on mica substrates. Monomeric SbpA dissolved in pure water was mixed with 10 mM tris(hydroxymethyl)aminomethane (Tris), pH 7.1, 100 mM NaCl, 50 mM $CaCl_2$ and injected into the fluid cell of an AFM equipped with a liquid-resistant, vertical engagement 160 μm scanner. The AFM probe consisted of a sharp silicon tip on a silicon nitride cantilever (HYDRA probe, length: 200 μm, spring constant $k \approx 0.035$ N/m, average tip diameter ≤ 15 nm, AppNano, Santa Clara, CA). Freshly peeled Mica discs (Grade V-1 Muscovite, Structural Probe, Inc) glued on metal disks using 20 min Epoxy glue were used as substrates for SLBs of POPC. For typical imaging conditions, AFM images were collected at scan frequencies of ≈1–8 Hz while applying a minimum loading force of ≈150 pN or less using optimized feedback and setpoint parameters for stable imaging conditions.

The dynamics of S-layer assembly on the SLB was investigated for a range of protein concentrations. The results, shown in **Figure 1**, revealed a multi-stage assembly pathway comprised of four distinct processes: (1) adsorption of extended monomers onto the SLB, (2) condensation into amorphous or liquid-like clusters, (3) rearrangement and folding into crystalline arrays of tetramers, and (4) growth by new tetramer formation at edge

Jim De Yoreo's research is directed towards understanding and manipulating interactions, assembly and crystallization in biomolecular and biomineral systems through the use of in situ AFM and TEM. He is currently the Chief Scientist for Materials Synthesis and Simulation Across Scales at Pacific Northwest National Laboratory (PNNL). He received his Ph.D. in Physics from Cornell University in 1985. Following post-doctoral work at Princeton University, he became a member of the technical staff at Lawrence Livermore National Laboratory (LLNL), where he held numerous positions. Prior to joining PNNL, he was the Interim Director of the Molecular Foundry at Lawrence Berkeley National Laboratory. He has served as President of the Materials Research Society (MRS), is a recipient of the Laudise Prize of the International Organization for Crystal Growth, and is a Fellow of the American Physical Society.

Raymond W. Friddle. Senior Member of Technical Staff, Sandia National Laboratories, Ray received his PhD from the University of California at Davis with a graduate fellowship from the Lawrence Livermore National Lab. Following post-doctoral work at the Molecular Foundry of Lawrence Berkeley National Lab, he became a senior member of the technical staff at Sandia National Laboratories in California. Ray's current work spans developing robust approaches to studying bi-molecular energy landscapes, the mechanics of metals at the atomic scale, and high-resolution imaging of conductive/insulator composites and hydrogen in metals.

Sungwook Chung received his PhD in Physical Chemistry from the University of California at Los Angeles in 2000. Following post-doctoral work at Northwestern University and Lawrence Livermore National Laboratory, he joined Lawrence Berkeley National Laboratory in 2008, where he has been a project staff scientist in Physical Biosciences Division and the Molecular Foundry. His research ranges from fabricating chemically and biologically driven nanostructures to investigating and manipulating the assembly process in biological and materials systems in situ.

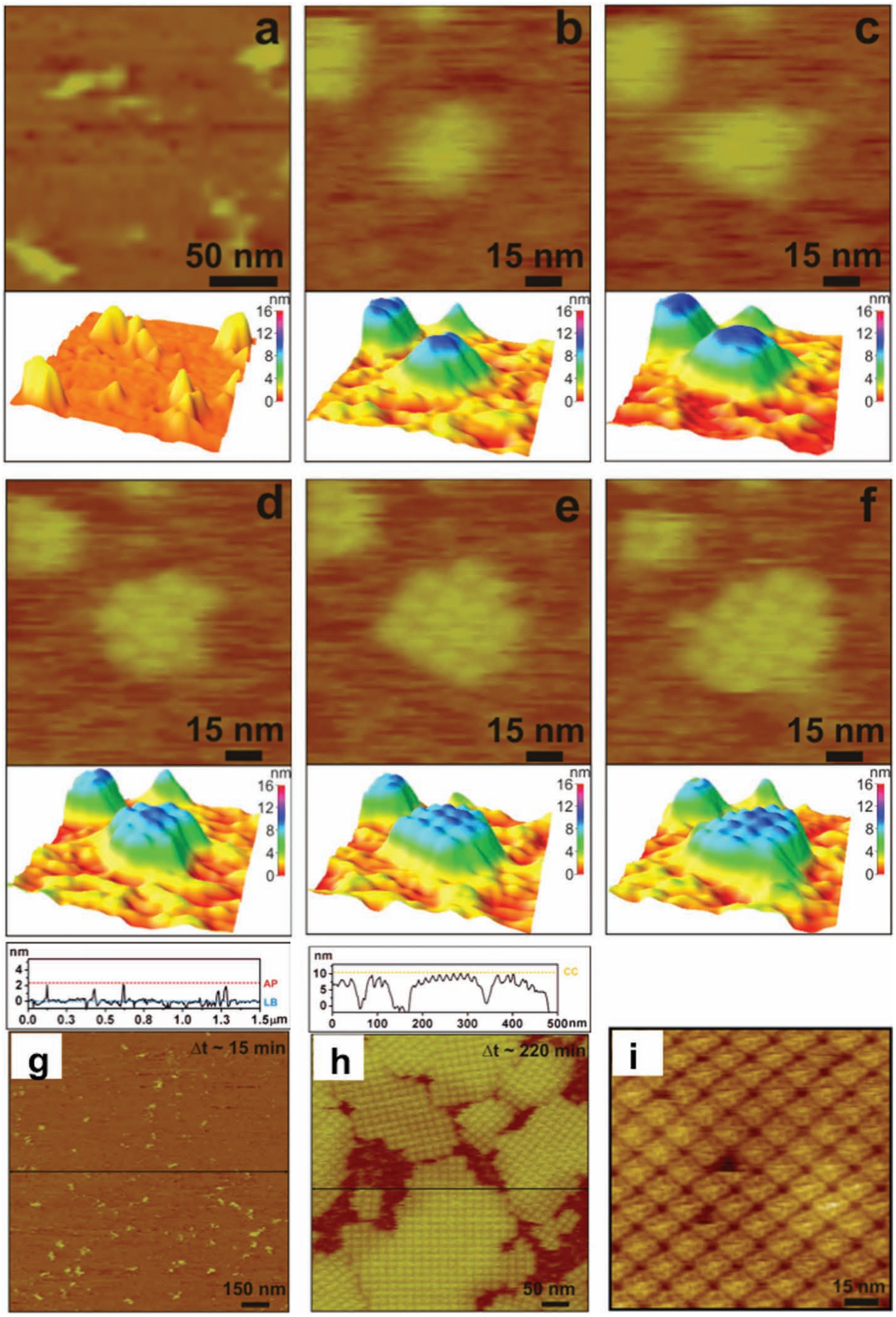

Figure 1. Sequential in situ AFM height images and surface plots showing the S-layer adsorption, followed by condensation and phase transition of a single cluster as well as its subsequent growth. Here, Δt indicates time elapsed since collection of the image in (a). a) At $\Delta t = 0$, monomers or small oligomers in an extended conformation have adsorbed to the SLB. b) By $\Delta t \approx 62$ min the amorphous nucleus has formed but shows signs of emerging order. Images at c) $\Delta t \approx 65.8$ min and d) $\Delta t \approx 70.3$ min show the phase transition from the amorphous (c) to crystalline (d) state, at which time each individual lattice unit is clearly discernable. After the transformation ((d) $\Delta t \approx 70.3$ to (h) 116.8 min), the crystal grows by formation of new lattice units at — and only at — unpopulated lattice sites along the perimeter of the crystal. For example, between d and e, newly formed lattice units complete the bottom and 3rd rows of the cluster. Times are (a) 0, (b) 62, (c) 65.8, (d) 70.3, (e) 88.5, (f) 95.5. (g, h) In situ AFM images and height profiles showing g) initial adsorbed proteins and h) fully crystalline clusters. Height profiles were measured along the horizontal black lines in each image and are labeled to denote the heights of the lipid bilayer (LB), adsorbed proteins (APs) and crystalline clusters (CCs). Here, Δt indicates time elapsed since introduction of protein solution. By $\Delta t = 15$ min (g), S-layer monomers had started to adsorb onto the SLBs and by $\Delta t \cong 87$ min, nearly all of amorphous clusters had transformed into CCs with a tetragonal lattice. At later times (e.g., $\Delta t \approx 220$ min, (h)), each CC continued to grow by consuming available APs near the cluster until growth was physically hindered by neighboring CCs. i) A highly-resolved image from mature CCs (g) reveals the tetrameric arrangement and sub-molecular details (i.e., loop-like structure) of the four S-layer monomers that comprise each lattice unit. Reproduced with permission.[12] Copyright 2010, National Academy of Science.

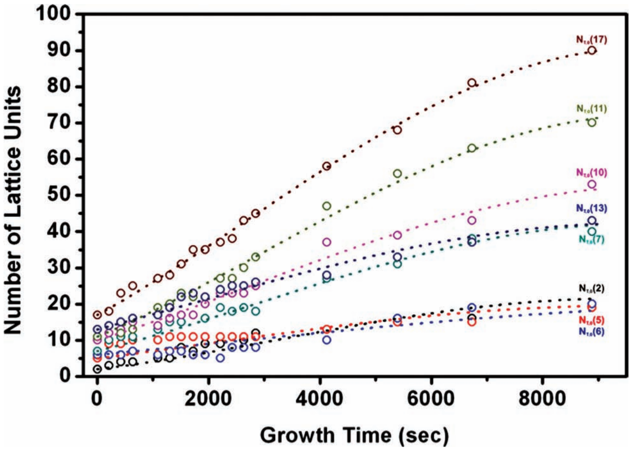

Figure 2. Growth rates of individual crystalline clusters for a range of initial sizes. They demonstrate that the growth rate for an individual cluster depends on its size at $t = 0$, with larger clusters exhibiting faster growth rates. $t = 0$ is time when the crystal phase appeared. Dotted lines give the fits to experimental data where the fitting was based on the model described in the text according to Equation (1). The legend relates the data for each curve to the initial number of lattice units in the crystal nuclei. Reproduced with permission.[12] Copyright 2010, National Academy of Science.

sites of the crystalline clusters. (A movie of the growth process can be found in the supplementary on-line information of ref. [12]). The in situ capability enabled Chung et al.[12] to measure cluster growth rates (**Figure 2**), which were then analyzed in terms of a model that assumed tetramer formation occurred at edge sites with a rate coefficient β controlled by diffusive transport of proteins along the lipid surface. This model gave a simple expression for the number of tetramers N_T in a cluster as a function of time;

$$N_T(t) = \left[\beta n_0 f(t) + N_{T,0}^{1/2}\right]^2 \tag{1}$$

where n_0 is the initial number density of monomers on the surface, $N_{T,0}$ is the number of tetramers in the cluster at the time of nucleation and $f(t)$ is a function that is linear at small t and approaches a constant at large t. The rate coefficient β was written as the product of the diffusive collision rate (aD/d), where a is the S-layer lattice parameter, D is the diffusivity and d is the typical jump distance of a few water molecules, and a Boltzmann factor $exp(-E_A/kT)$, in which the activation energy E_A is associated with the creation of new tetramers. This analysis led to an estimate for E_A of about 50 kJ/mol or 20 kT, which is about half of the free energy barrier expected for folding of a single protein the size of SbpA.[17] Consequently, the ability to image assembly in situ revealed an auto-catalytic process in which the emergence of order in the S-layer cluster reduces the barrier to forming the next ordered growth unit.

Shin et al.[13] followed this study by examining the role played by the substrate. They followed S-layer assembly on bare mica and found that, in the absence of the lipids, two distinct structural domains of S-layers are formed. One is identical to that observed on the SLB. The second, however, is 2–3 nm shorter in height, though the lateral dimensions of the lattice are identical or nearly so (**Figure 3**A). Over time, the short domains transformed into the tall domains by "standing up", as shown in Figure 3B. The ability to investigate this system in situ enabled quantification of the number density of nuclei that formed the short and tall phases and thus extract the relative magnitude of the barriers to nucleation of each. Taking $N_S/N_T = exp(-(E_S-E_T)/kT)$, where N_i and E_i are the fractions of clusters and activation barriers, respectively, and the subscripts S and T refer to short and tall, from analysis of the data the difference between the two barriers ($\Delta = E_S-E_T$) was found to be only 1.6 kJ/mol or 0.7 kT,[13] which is much less than the barriers given above to creating new tetramers either through isolated protein folding or new tetramer formation at S-layer boundaries.

Analysis of the rates of transformation form short to tall showed that, in contrast to the small difference in the probability of forming short and tall phases, the barrier to transformation is quite large. The number of short domains at any time is given by $N_S(t) = N_S(t = 0)exp(-t/\tau)$ where $N_S(t = 0)$ is initial number of short domains before transformation and $1/\tau$ is the characteristic rate coefficient and $1/\tau = f\,exp(-E_B/kT)$ where f is the characteristic attempt frequency associated with conformational fluctuations and E_B is the barrier to transformation. As **Figure** 4A shows, the fraction of short domains does indeed follow a simple exponential dependence. Assuming the transformation of an entire domain is triggered by transformation of a single tetramer (see Figure 3B) and taking an appropriate value for f,[13] that barrier was found to be 61 kJ/mol or 25 kT. Thus, once the high-energy domains form, the barrier to their relaxation into low-energy domains is nearly as great as the barrier to folding of individual S-layer proteins.

The findings of these two studies of S-layer crystallization highlight the value of in situ AFM observations. They revealed the complex nature of the nucleation and growth pathway, demonstrated the importance of kinetic traps in determining that pathway and provided quantification of the energy barriers controlling formation rates (Figure 4B). They also led to a realization of the similarity between the dynamics of protein folding and the assembly of proteins into extended ordered structures that require the individual constituents to undergo conformational changes. When individual proteins transform from an unstructured state to the final equilibrium state, the concept of a folding funnel characterized by a large number of potential initial states higher in energy than the final state (**Figure 5**) is often invoked.[18] The walls of the funnel are presumed not to be smooth and the resulting bumps and valleys define kinetic traps where the protein exhibits non-equilibrium structures for extended periods of time. These transient structures can be disordered "molten globules" or partially ordered intermediates.[19] From these studies on S-layer assembly dynamics, we see that the concept of the folding funnel for individual proteins can be equally applied to assembly of extended ordered protein structures. Beginning with rapid collapse into clusters of monomers, the S-layer system explores many configurations before transforming into the final ordered state. However, a large percentage of the trajectories render the system temporarily trapped in a high-energy, less ordered structure, from which it slowly relaxes into the low-energy equilibrium structure. Indeed, the language used to describe the protein folding funnel is well suited to this picture of S-layer assembly, with the amorphous liquid-like clusters investigated in our previous study representing the multi-protein equivalent of the "molten globules" and the partially ordered high-energy domains constituting the "folding intermediates". Because extended protein architectures with

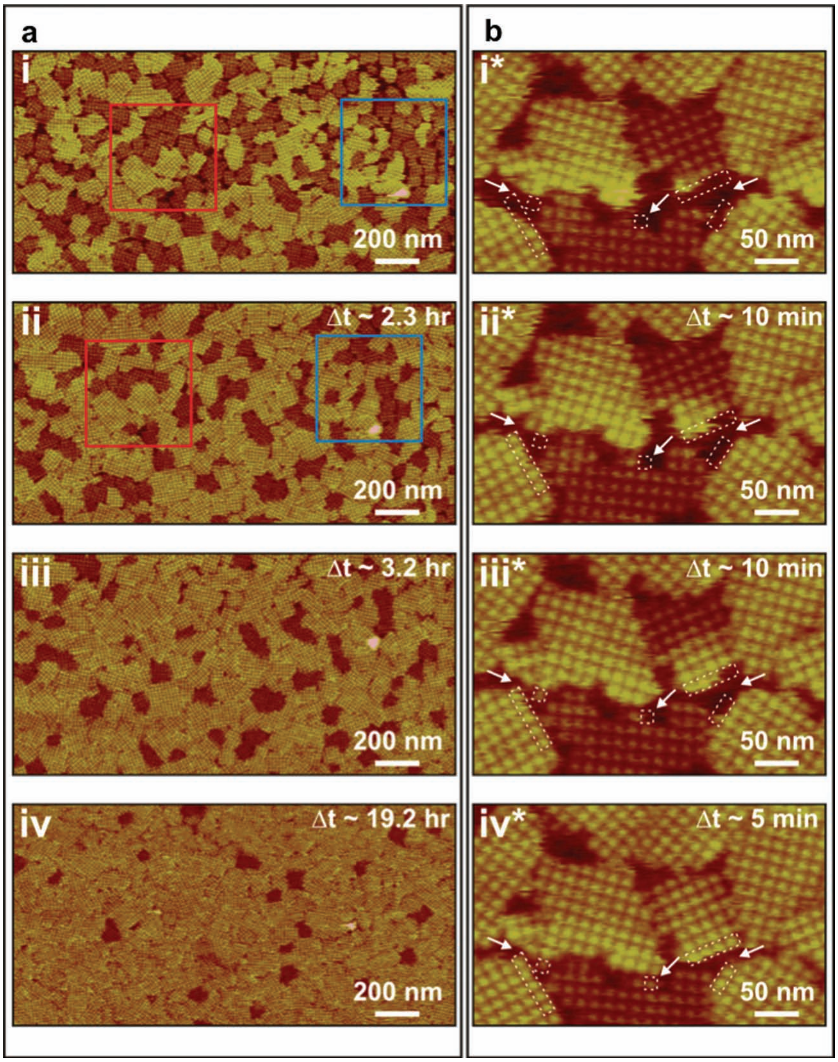

Figure 3. Sequences of in situ AFM images of 2D S-layers assembled on mica showing the two types of domains, as well as the transformation from short to tall domains. Δt indicates time elapsed since collection of images i and i*. S-layer crystals were initially grown in solution at 25 °C and further development of the domains was monitored in the same solution. Series in (a) shows evolution in distribution of domains in protein solution following an incubation time of 4.5 h. (i) Initial ratio of tall to short domains by area was 1.3. (ii) By $\Delta t \approx 2.3$ h, about 25% of the short domains in (i) had transformed into tall domains without any dissolution of S-layer proteins from the domains. (iii) and (iv) At $\Delta t \approx 3.2$ and 19.2 h, most of the short domains had transformed into tall domains. However a few short domains still remained, indicating that the transformation does not go to 100% completion until much later times. Series in (b) shows transformation of a single domain in protein solution following an incubation time of 2.5 h. The transition began at the free edge of the short domain. In between (iii*) and (iv*), the short domain continued to grow by adding new tetramers at the bottom edge. Times of image collection were (i*) 2.5, (ii*) 2.7, (iii*) 2.8, and (iv*) 2.9 h. Reproduced with permission.[13] Copyright 2012, National Academy of Science.

long-range order commonly require conformational changes from the monomeric structures, this picture may be generally applicable the phenomenon of protein self-assembly.

3. Biomineralization

The complex shapes, hierarchical structures and unique properties found in biominerals have long captured the imagination of crystal chemists. Early attempts to understand how ionic crystals with classical shapes and poor mechanical properties could be so remarkably different when formed by organisms were focused mainly on the changes seen in crystal morphology.[21] These studies typically examined crystals grown in the presence of proteins extracted from organisms at sites of mineralization[22] as well as peptides and other small molecules expressing functional groups similar to those present in the full proteins.[23,24] By comparing shape changes to the molecular structures of the modified crystal surfaces, particularly those of newly expressed faces, the investigations postulated the nature of the dominant interactions and stereochemical relationships responsible for the altered crystal shapes.

While more recent investigations have shown that the initial formation process of many and perhaps all biominerals occurs along a complex pathway involving disordered or amorphous precursors,[25,26] the significance of biomolecule-biomineral interactions continues to be a subject of intensive study. Protein-mineral interactions are believed to be involved in stabilization of non-equilibrium phases[27] and control over mineral shape,[28] and protein incorporation plays a major role in determining mechanical properties.[29] In situ AFM has contributed significantly to developing a mechanism-based understanding of these phenomena. By examining the atomic-scale dynamics of crystal growth, AFM studies have provided a link between growth modification and the underlying chemical interactions.[30–35]

Of the numerous mechanisms of modification identified by AFM, a central theme has been the link between biomolecule-step interactions and changes in growth dynamics that influence mineral phase, growth rate, crystal shape, and incorporation of organics. One of the most important factors to emerge as a key control on the effect of biomolecules is the stereochemical relationship between the step and the organic modifier. The effects of citrate on the growth of the crystal calcium oxalate monohydrate (COM, CaC_2O_4 H_2O) provides an excellent example. COM is the main mineral phase of human urinary stones and citrate is both a naturally occurring inhibitor and a therapeutic often prescribed to kidney stone patients. **Figure 6** shows the changes in the shape of a typical COM crystal as the concentration of citrate in solution is increased.[36] Also shown is as the evolution in growth hillock morphology during growth of the $(\bar{1}01)$ and (010) face of COM in the presence of citrate. In contrast to the minor effects on the (010) face, extreme changes are observed on the $(\bar{1}01)$ face. In particular, the [101] step shows a dramatic reduction in step speed and extreme step edge roughening.

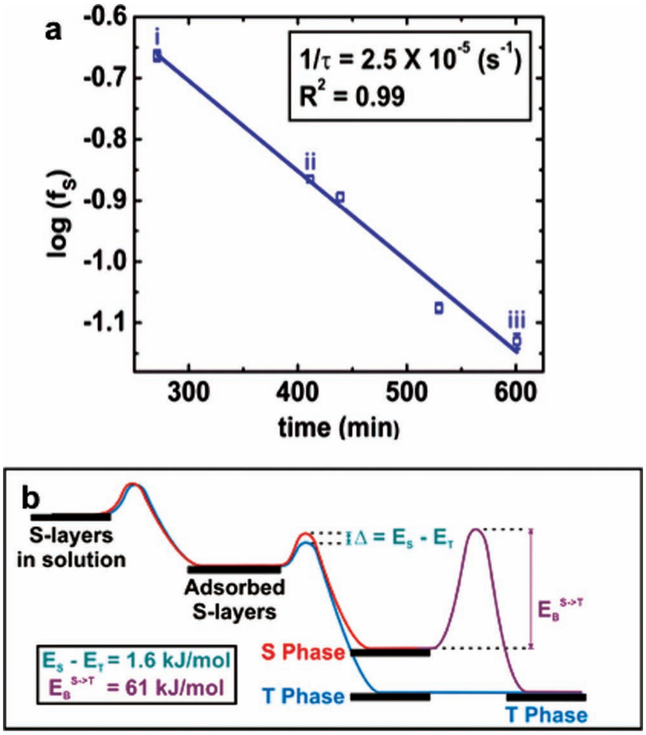

Figure 4. a) Kinetics of short-to-tall S-layer domain transformation on bare mica and associated energy diagram. The plot gives the relative number ratio of short domains (f_s) vs. time showing a simple exponential dependence. The best linear fit is shown as a solid line. From these data, the energy barrier to transformation of a domain from short to tall was found to be about ≈61 kJ/mol. Labeling of data points (i - iv) corresponds to the image in Figure 3a on which the analysis was performed. Solid line gives a guide to the eye. Times at which images were captured are (i) 4.5, (ii) 6.8, (iii) 10.0, and (iv) 29.2 h. (b) Proposed energy diagram of S-layer assembly from the monomer in solution to the crystal on mica. Energy barriers to formation of two states only differ by 1.6 kJ/mol however the energy barrier to transformation from one to the other is ≈ 38 times larger. These energy barriers are qualitatively presented along with two pathways during the assembly. Reproduced with permission.[13] Copyright 2012, National Academy of Science.

Figure 6 demonstrates that the macroscopic shape change is a direct reflection of the atomic-scale changes in step morphology.

Figure 7 shows the results of molecular models that predict the optimized citrate binding configuration at the dominant steps on the two faces. These models reveal the importance of stereochemistry at step edges by showing that the binding energy of citrate is considerably higher at any step than it is to either of the flat faces[33] (73 to 167 kJ/mol vs. 49 to 65 kJ/mol). Moreover, the step that is most strongly affected by addition of citrate, the [101] step on the $(\bar{1}01)$ face, has by far the highest binding energy (–166.5 kJ/mol). The predicted geometry of citrate binding to this step is shown in Figure 7A.[33] The stereochemical relationships seen in the simulations reveal the importance of both the orientation of oxalate groups, which can repel the citrate carboxyl groups, and the configuration of calcium sites on the crystal surface, to which the carboxyl groups can bind electrostatically. The geometry of the acute [101] step on the $(\bar{1}01)$ face provides the most favorable steric configuration because it optimizes both factors.

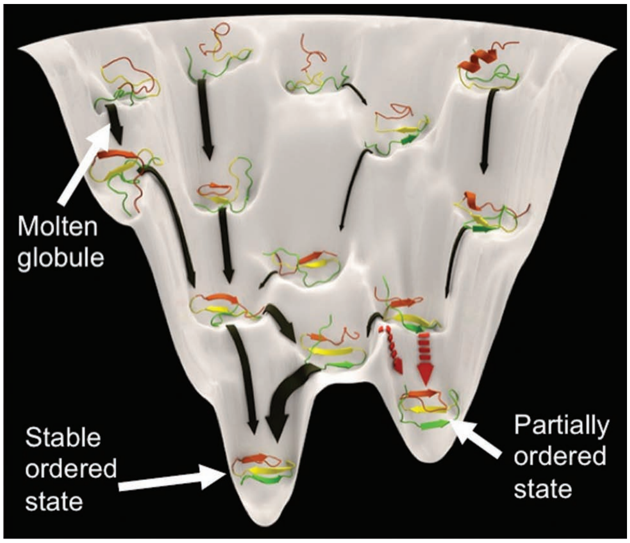

Figure 5. Protein folding funnel showing unfolded, molten globule, partially ordered state and fully ordered state. Barriers to forming partially ordered and fully ordered state from molten globule are small, but barrier to transformation from partially ordered to fully ordered states is large.[20]

By comparison, binding energies for citrate to all steps on the (010) face are much less favorable, with binding to the $[\bar{1}00]$ step predicted to be only –73.2 kJ/mol, or over 2× smaller than for the [101] step. The predicted geometry of citrate binding to the $[\bar{1}00]$ step is shown in Figure 7B. The extension of dicarboxylic acids of oxalate molecules beyond the (010) plane causes electrostatic repulsion and thereby makes it difficult for citrate molecules to bind to the steps or to the face. Thus, binding energies for these steps are also consistent with the very minor effects of citrate on the (010) face.[32,33]

The morphological result of strong citrate binding to the [101] step is that its edge becomes serrated as citrate pins the step at many sites along its length.[32] As a step segment tries to advance between two pinning sites, it becomes curved. According to Gibbs–Thomson relationship, the equilibrium solubility of a solid is an increasing function of the surface curvature.[37] The same rule applies to steps. Thus even in a solution supersaturated with respect to the bulk crystal, a step segment between two pinning sites will only advance until it reaches a curvature for which it has the same chemical potential as the solution.[37] At low supersaturation (σ) or high citrate concentration (C_i), the result is complete inhibition. At sufficiently high supersaturations or low citrate concentration, the step can advance, but does so more slowly than in the pure system because the citrate molecules adsorbed to the step edges have eliminated sites for solute attachment — so-called kink sites.

With these two basic ideas — curvature-dependent solubility and kink site blocking — the in situ growth data enabled development of a quantitative model for growth modification. **Figure 8** shows the measured dependence of [101] step speed in the presence of the impurity (v_i) divided by the step speed in pure solution (v_0) on citrate concentration for a range of Ca^{2+} activities $a_{(Ca)}$ along with the predictions of a model that includes the effects of step pinning and kink blocking according to.[35]

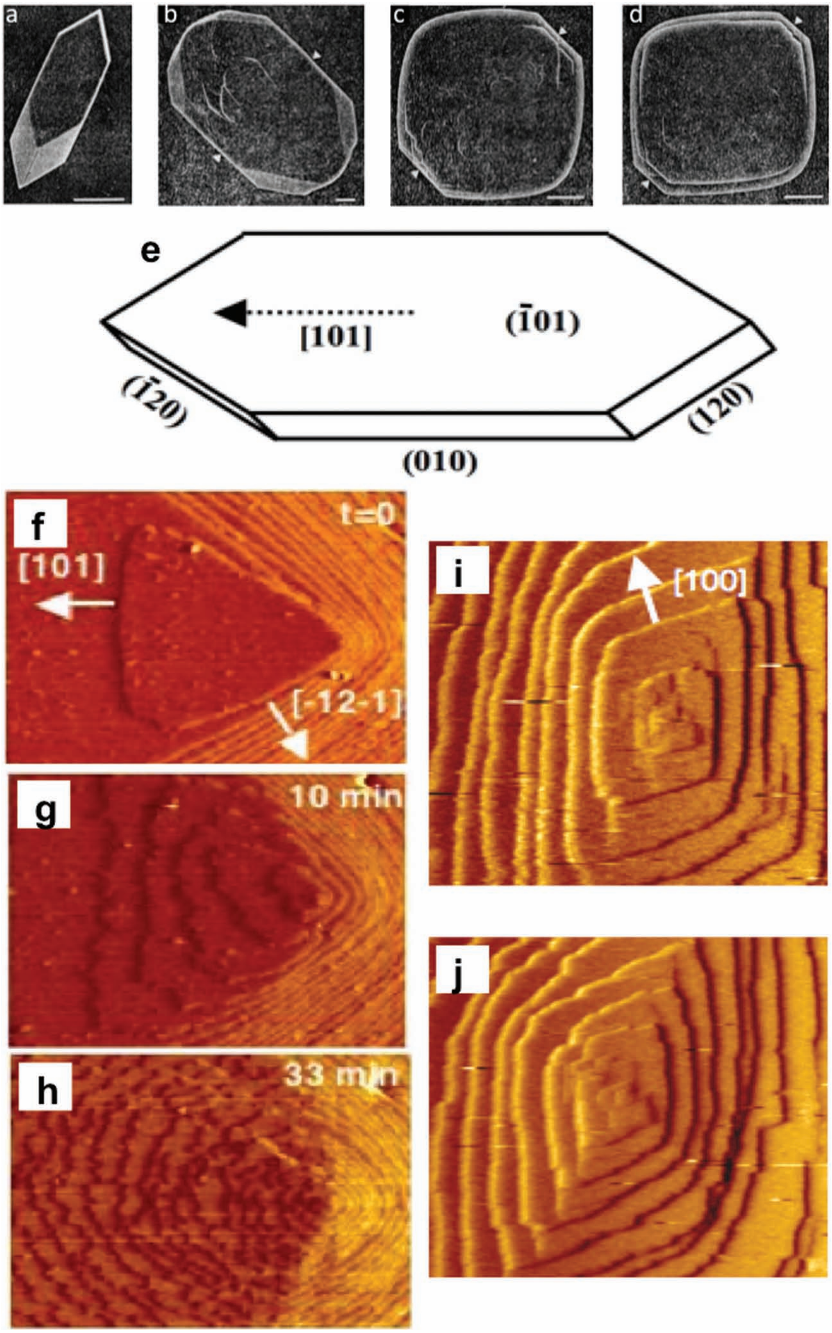

Figure 6. Scanning electron micrographs of COM crystals formed in pure supersaturated calcium oxalate solution (a) and in the citrate-bearing solutions at various citrate concentrations; 10^{-4} M (b), 10^{-3} M (c), and 2×10^{-3} M (d). Scale bar: 10 µm. (Courtesy of the Journal of Urology (55).) e) A geometrical model illustrating the COM crystal with its distinguished facets. f–h) Effect of citrate on morphology of the $(\bar{1}01)$ face during growth. Sequential AFM images during growth in citrate-bearing solution at $t = 0$ min. (f), $t = 10$ min. (g), and t = 33 min (h). Because the speed of the [101] step is more strongly affected than the [120] steps, its speed drops more dramatically and thus the terrace widths become nearly equal in the two directions. Image sizes: 4.1 µm × 3.3 µm. i, j) AFM images showing growth hillocks on the (010) face in pure (i) and citrate-containing (j) solutions. Image sizes are 1.2 µm × 1.2 µm. Reproduced with permission.[32] Copyright 2004, National Academy of Science.

$$v_i/v_0 = \left\{1 - A_3\left[\frac{A_2C_i}{1+A_2C_i}\right]^{0.5}\right\}\left\{1 - \frac{e^{A_1\left[\frac{A_2C_i}{1+A_2C_i}\right]^{0.5}} - 1}{e^{\sigma} - 1}\right\} \quad (2)$$

where A_2 is just the ratio of the adsorption to desorption rate coefficients (K_A/K_D) in the expression for Langmuir adsorption, A_3 contains the kink density in the pure system, as well as some geometric factors, and A_1 includes some materials parameters, geometric factors, and the impurity-step sticking coefficient. The first term in Equation (2) captures the kinetic inhibition created by blocking of kink sites by the impurities and the second term gives the thermodynamic inhibition caused by step curvature between impurity pinning sites. The data are well fit by this model and show that the step-specific inhibition and resulting change in crystal shape are due to a combination of thermodynamic effects from step curvature and kinetic effects from kink blocking. Moreover the combined results from the AFM experiments and MM calculations provide the desired link between the mechanistic change in growth behavior and the underlying energetics of the crystal-modifier interaction.

The introduction of highly-acidic long-chain peptides or proteins, which are often found in association with biominerals, introduces a new set of phenomena associated with two characteristic features, whose effects can only be realized through in situ studies. The first is the tendency to aggregate into clusters on charged surfaces[38] and the second is the dynamic nature of surface binding,[39] both in terms of the relatively long timescale for peptide adsorption to the surface and the tendency to weakly adsorb before relaxing to a more strongly bound state. Friddle et al.[31] investigated the unique behavior of long-chain peptides by examining COM growth in the presence of $(DDDS)_6DDD$. These were chosen to act as surrogates for the Asp-rich region of osteopontin, which is an acidic urinary protein containing 19 Asp residues occurring primarily in groups of two-to-three. OPN is known to strongly inhibit COM growth in vitro.[40]

To investigate this system at the highest resolution, Friddle et al.[31] employed two modifications of the standard approach to imaging crystal surfaces by AFM. Capturing the morphological evolution of atomic steps and their interaction with soft, weakly-adsorbed macromolecules requires rapid scanning. Thus cantilever stiffness must be low to minimize the force applied as it passes over topographic features such as steps and macromolecules. At the same time, high-resolution imaging requires sharp probes. Silicon probes, which offer excellent sharpness, are too stiff to scan at high rates in contact mode without displacing adhered

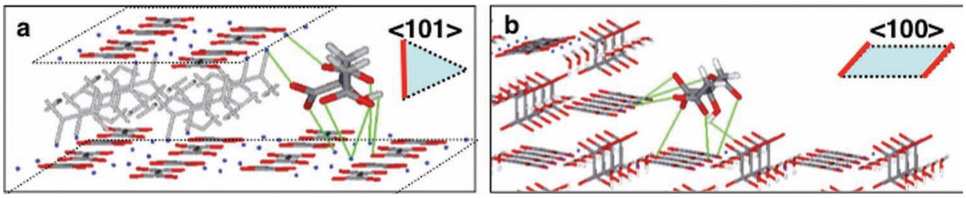

Figure 7. Geometry of citrate binding to steps in minimum energy configuration. a) citrate molecule bound to acute [101] step on ($\bar{1}01$) face. The calculated binding energy is –166.5 kJ/mol. b) citrate molecule bound to ($\bar{1}00$) step on (010) face. The calculated binding energy is –73 kJ/mol. The large difference in binding energy is due to a mixture of electrostatic and stereochemical factors. Reproduced with permission.[33] Copyright 2005, American Chemical Society.

molecules or fracturing the brittle tip. The common solution is to use cantilever probes fabricated from silicon nitride, which are much softer; but the malleability of silicon nitride renders these probes dull and limits their resolving power. To overcome these limitations, as in the work on S-layers described above, Friddle et al.[31] employed probes comprised of sharpened Si tips on flexible, low-stress Si_3N_4 cantilevers (Applied Nanostructures, CA). To augment the relatively weak laser signal reflected from the thin Si_3N_4 cantilever beam (600 nm thick, uncoated) they utilized a 3 mW diode laser instead of the ≈1 mW laser usually employed.

Figure 9A,B show the atomic resolution images of the COM ($\bar{1}01$) and (100) surfaces obtained by employing these modifications to the imaging procedure. Image enhancement by Fourier filtering revealed sub-molecular details such as protruding ends of vertically aligned oxalate groups (high "peaks") and recessed, flat-lying oxalate groups (low "holes") (Figure 9A) on the (010) face. Comparison of Figure 9A,B shows the greater vertical relief of the (010) face as compared to the ($\bar{1}01$) face. The overlying molecular models show the electrostatic maps for the lowest energy configuration of $(DDDS)_6DDD$ binding to these two faces based on classical molecular dynamics (MD) simulations. The negative oxygen atoms of the oxalate ions that protrude from the (010) terrace are predicted to repel the negative carboxyl side groups along the peptide (Figure 9A), while the positive calcium-rich ($\bar{1}01$) terrace provided a favorable binding environment (Figure 9B). Thus peptide binding to the ($\bar{1}01$) face was predicted to be nearly three times greater than to the (010) face.

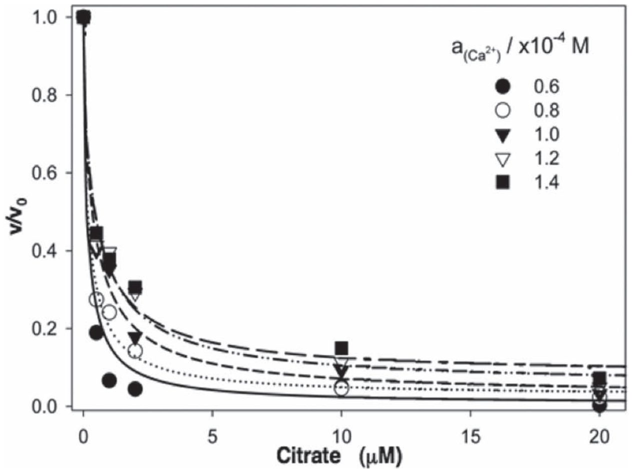

Figure 8. Dependence of ν/ν_0 on citrate concentration for a range of Ca^{2+} activities. Lines are fits to the data according to model described in text and described by Equation (2). Reproduced with permission.[33] Copyright 2005, American Chemical Society.

Indeed, as expected from MD simulations, the peptides bound to the ($\bar{1}01$) face so that, even at peptide concentrations <10 nM, the face was covered with a film of peptides and the lattice was no longer resolvable (Figure 9C). In contrast, the (010) atomic structure was still well resolved, showing that *individual* peptides did not bind to that face (Figure 9D). Instead, despite the like-charge of the peptides and the face, the peptides formed surface-adsorbed clusters about 10 nm in size (Figure 9D). By following the step dynamics at molecular resolution, Friddle et al.[31] found that these contrasting adsorption behaviors led to distinct, face-specific controls on growth (**Figure 10**). On the ($\bar{1}01$) face, as steps moved through the adsorbed peptides, they became severely roughened due to a high density of pinning sites. But on the (010) face, the steps still consisted of straight segments with visible kinks. When a step encountered a peptide cluster, it formed a hinge-point where it was temporarily stopped. Eventually, the steps overcame these obstacles and recovered to their straight morphology, leaving the peptide clusters unperturbed by the passing step. This process occurred repeatedly without any significant change to cluster location or shape (movies of these growth processes are provided in the supplementary on-line information to ref. [31])

Measurements of step speed ν on the ($\bar{1}01$) face revealed a number of consequences of peptide adsorption dynamics. First, the steps exhibited two distinct states: Upon decreasing supersaturation σ from high values, ν suddenly jumped from that of the pure system into a "dead zone", i.e., a region of finite supersaturation in which no growth occurs. (Figure 9E, red, yellow, green curves). But upon increasing σ from near-equilibrium values, ν followed a smooth trajectory with no abrupt changes (Figure 9E, blue curve). Moreover, as Figure 9F shows, at the supersaturation where the step speed jumped to zero, ν fluctuated between the two predicted end-states.

This phenomenon of bi-stable growth observed on the ($\bar{1}01$) face was proposed to be a natural consequence of polypeptide adsorption kinetics on faces to which they strongly bind through specific interactions. The series of barriers that slow the adsorption of polypeptides[41] results in their passage through multiple configurations before reaching a lowest-energy collapsed state.[39] Under supersaturated conditions, step growth competes with this slow peptide binding: When

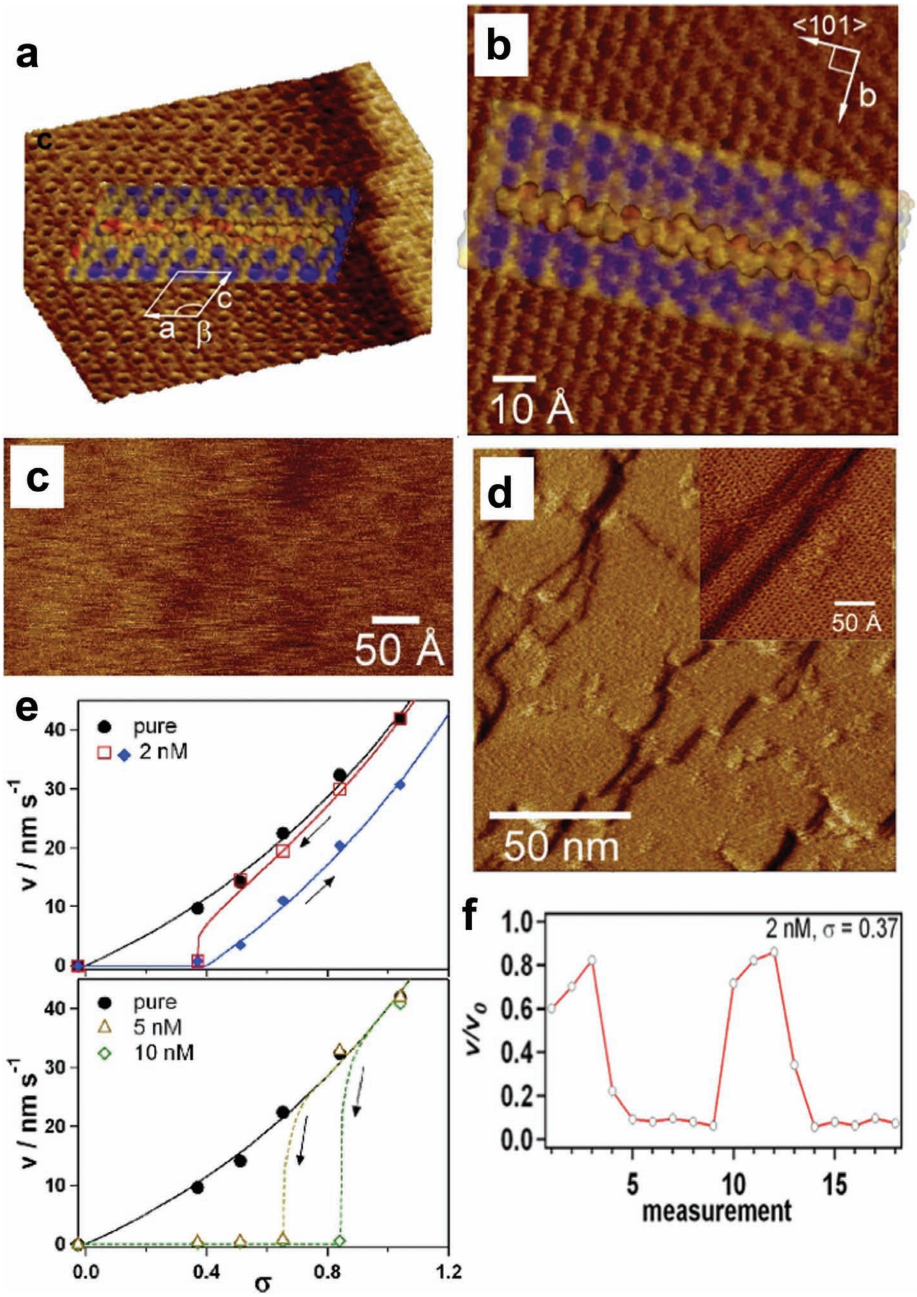

Figure 9. a) AFM deflection image of ($\bar{1}01$) face and electrostatic map for configuration of highest binding energy for $(DDDS)_6DDD$ as predicted by the in vacuo MD simulations. b) AFM deflection image of (010) face showing step, kinks and electrostatic map of $(DDDS)_6DDD$ for configuration of highest binding energy. Red is most negative, blue is most positive. In an intuitive and simple electrostatic picture of binding, the negative (yellow) oxygen atoms of the oxalate ions that protrude from the terrace are expected to repel the negative (yellow-to-red) carboxyl side groups along the peptide. In contrast, on the ($\bar{1}01$) face, the MD simulations predict the positive (blue) calcium-rich terrace should provide a favorable binding environment for the carboxyl-rich peptide. Unit cell parameters (9) are $a = 9.976$ Å, $b = 14.588$ Å, $c = 6.291$ Å, and $b = 107.05°$. Electrostatic potentials in c and d were rendered using MOE 2005.06 (Chemical Computing Group, Montreal, Canada). Molecular structures in panels a and b were rendered using WebLab ViewerPro 3.7 (Molecular Simulations, San Diego, CA). c) High resolution image showing that, unlike the (010) face, the ($\bar{1}01$) face becomes covered by a uniform film of peptide preventing visualization of the underlying lattice ($(DDDS)_6DDD$). d) Morphology of (010) face during growth in 5 nM $(DDDS)_6DDD$ showing peptide clusters and pinned steps. Inset shows, high resolution image of one peptide cluster in front of approaching steps and one within with the upper step. The crystal lattice is well resolved and the adsorbed peptides are confined to the clusters. e) Step speed versus supersaturation for various concentrations of $(DDDS)_6DDD$. Symbols are experimental values taken after introducing the indicated peptide concentration into otherwise pure solution. Red squares and blue circles were collected while reducing and increasing supersaturation, respectively. Standard errors are smaller than the symbols. Solid curves give the theoretical dependence that takes into account the slow adsorption kinetics of the peptides for decreasing (downward arrow) and increasing (upward arrow) supersaturation. f) Series of individual step speed measurements showing bi-stability for $\sigma = 0.37$ and a $(DDDS)_6DDD$ concentration of 2 nM. Reproduced with permission.[31] Copyright 2010, National Academy of Science.

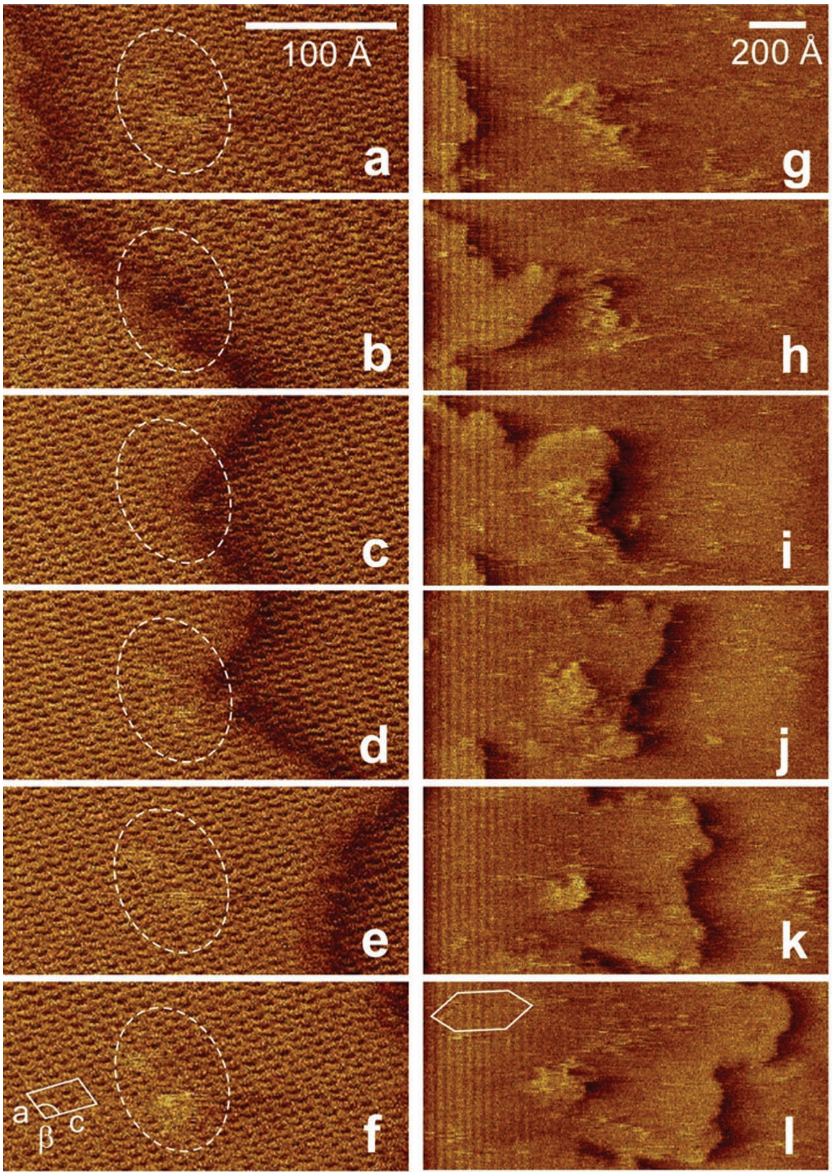

Figure 10. a–f) Series of sequential images showing interaction of step on (010) face with peptide clusters in a solution containing 10 nM DDDS ($I = 0.15$ M). An individual step approaches two adjacent clusters (a,b), is transiently pinned (c,d), and then recovers (e,f). Frame interval 4.2 s. g–l) Time sequence showing inhibited growth of step on $(\bar{1}01)$ face. A single large peptide aggregate near the center of the image provides a point of reference. The continuous film of peptides on this face transiently pin sub-segments of the oncoming step at many sites along the step front. Frame interval 8.4 s. Note the sudden extension of the step towards the reference cluster in (h), followed by inhibition of the same step region in (i). This behavior of slight acceleration as steps approach clusters was often observed on both faces. Reproduced with permission.[31] Copyright 2010, National Academy of Science.

an approaching step arrives at a peptide binding site, if the peptide is well-bound, it can block solute access to kinks; but if it is weakly adhered, as the peptide bonds to the crystal fluctuate, step-propagation can proceed past the site. Thus, whether a peptide impedes step motion depends on the characteristic timescale t available to relax into the well-bound state.

The time window for peptide binding is the terrace exposure time T, which is given by L/v where L is the distance between steps. Analysis of the step speed data on the $(\bar{1}01)$ face shows that the characteristic time t for $(\mathrm{DDDS})_6\mathrm{DDD}$ adsorption is ≈40 s and, at the higher values of σ used in these experiments, $T<<t$.[34,42] However, because L and v decrease and increase with supersaturation, respectively, upon reduction of σ, T rapidly increases. When sufficiently low σ is reached, the coverage of well-bound peptides is then large enough to appreciably slow the steps. As they slow, T increases further resulting in yet higher peptide coverage, which again reduces v, raising the peptide coverage yet again, and so on. Because of this positive feedback, step speed exhibits the characteristic feature of a mathematical "catastrophe",[43] i.e., there is a point at which v spontaneously jumps from a finite value to zero and does not exhibit intermediate values. In contrast, when the crystal is first exposed to peptides at a value of σ below the jump, step speed is near zero ($T>>t$) and peptide adsorption proceeds unperturbed until equilibrium coverage of well-bound peptides is reached. Even as σ increases, they present a large barrier to desorption that steps cannot overcome. As a consequence, the dynamic relation between timescales is lost and v follows a trajectory well-predicted by the classic pinning model described for citrate inhibition of COM[35] *in the absence of time dependent adsorption*.

Thus the slow, multi-state binding of peptides to the $(\bar{1}01)$ face breaks the symmetry in the step kinetics: Upon decrease of σ from high levels, weakly-bound peptides are displaced by rapidly advancing steps, but upon increase from equilibrium, they present nearly-permanent adsorbates, the symmetry is broken and the step exhibits two distinct states — uninhibited growth or arrested growth. Because the surface peptide coverage will increase with solution peptide concentration, the supersaturation at which the jump between states occurs should also increase, as is observed experimentally. The red and blue curves in Figure 9E give the predictions of this model for a two-state adsorption mechanism in which peptides first adsorb in a weakly bound state and then relax to a well-bound state. These findings demonstrate how the inherent ability of in situ AFM to probe system dynamics enables an understanding of the complex nature of protein-mineral interactions.

4. Measuring Biomolecular Interactions

Ultimately, the ability of substrates or soluble biomolecules to alter pathways of protein assembly or biomineralization, the kinetics of nucleation and growth, or the final morphology of the products, depends on the strength of protein-protein and protein-surface interactions. Dynamic force spectroscopy (DFS), which measures the force required to pull an AFM tip off of a surface as a function of pulling rate, has provided researchers the ability to characterize the microscopic basis of inter- and intra-molecular bonding.[44–46] The technique is rooted in the early works of Eyring[45,47] and Zhurkov[48] where the failure times of stressed materials were explained through Arrhenius-like models of thermal activation over energy barriers. This microscopic view was scaled down further by Bell,[49] and later Evans[50] to analyze the failure of single-molecule bonds under stress. Evans and co-workers performed a thorough analysis of bond breaking dynamics that included model potentials and bonding scenarios,[44,51] and found that the typical rupture force of a single bond varies as the logarithm of the loading rate, $f \approx \ln r$, when it is driven far from equilibrium, where $r = df/dt$ is the rate of increasing force with time. This model has served as a foundation for the modern analysis of force spectroscopy experiments, in which the data, arranged as a plot of the rupture force vs log-loading rate (the force spectrum) are expected to form a straight line, at least for irreversible rupture of a single bond over a single energy barrier. The slope of the line provides information about the characteristics of the bond.

Recently, Friddle et al.[52] showed that force spectroscopy carried out over a sufficiently wide range of pulling rates naturally explores both this far-from-equilibrium regime as well as a near-equilibrium regime and that the measured rupture force exhibits a characteristic non-linear dependence on log-pulling rate across the two regimes. For a single bond, they found that the spectrum of rupture forces is given by

$$\langle f \rangle \cong f_{eq} + f_\beta e^{\frac{1}{R(eq)}} E_1\left(\frac{1}{R(f_{eq})}\right) \quad R(f_{eq}) = \frac{r}{k_u(f_{eq}) f_\beta} \tag{3}$$

where $f_\beta = k_\mathrm{b}T/x_t$ is the thermal force scale, and $E_1(z) = \int_z^\infty \frac{e^{-s}}{s} ds$ is the exponential integral and

$$f_{eq} = \sqrt{2k_c \Delta G_{bu}} \tag{4}$$

defines the equilibrium force for the bond/transducer system, where k_c is the cantilever force constant and ΔG_bu is the free energy of binding. For multiple bonds, the dependence follows a qualitatively similar trend, though the details of $<f>$ and f_eq differ.[52] **Figure 11** shows this characteristic dependence for the ten different molecular bonds and the inset shows that, in the natural variables of the system, all force spectra fall on a universal curve. Hence, by collecting bond rupture force data over a sufficiently wide range of pulling rates, the equilibrium property of binding free energy can be extracted.

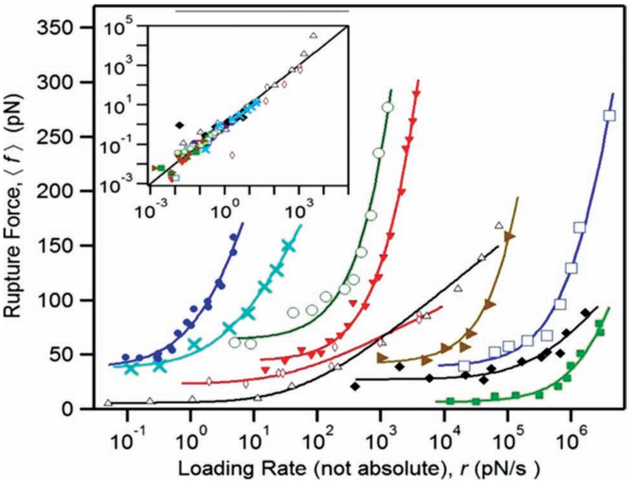

Figure 11. Model fits to the nonlinear force spectra of intermolecular bonds. Force spectra of 10 data sets taken from the literature are fit to N-bond analogue of Equation 3 assuming a generic equilibrium force and apparent transition state distance. Data are exploded along the loading rate axis for clarity. Inset: The same data plotted in the natural coordinates show that all spectra collapse onto a single line. Bond and reference legend are as follows: green open circles, Aβ-40/Aβ-40; blue open boxes, peptide/steel; blue x's, integrin/fibronectin; solid orange triangles, lysozyme/anti-lysozyme; solid red triangles, LFA1/ICAM1; solid black diamonds, Si_3N_4/Mica in ethanol; open red diamonds, Dig/Anti-Dig; solid blue circles, N,C,Npincer/pyridine; solid green squares, actomyosin/ADP, open black diamonds biotin/avidin. Reproduced with permission.[52] Copyright 2012, National Academy of Science.

To perform DFS measurements, the AFM tip is functionalized with one of the two molecules of interest and the other is immobilized on a surface. To carry out true single molecule binding experiments, the coverage on the AFM tip to be sufficiently low that most measurements give no result so that those that do are likely to represent single molecule bonds. Alternatively, high coverage can be used and multi-bond spectra collected. Although absolute values of the binding free energy cannot be extracted from such data without knowing the number of bonds N, relative values for multiple surfaces can still be obtained, because small differences from tip to tip have a negligible effect on the accuracy of the measurement when N is large.

The chemistry used to functionalize tips and surfaces depends on the system of interest, however a typical approach used for peptide and protein functionalization developed by Friddle et al.[53] is as follows. Bare Si_3N_4 AFM tips are cleaned under UV/ozone for 10 min, then immersed in acetone for 30 min, rinsed in ethanol, then dried under a nitrogen stream. Cleaned tips are coated with 4 nm Cr followed by 40 nm Au by thermal evaporation. These probes are then immersed for 30 min in a DMF solution containing 0.2 mM of the heterobifunctional cross-linker LC-SPDP (Thermo Scientific) consisting of a pyridyl disulfide, which adsorbs to Au, and an N-hydroxysuccinimide (NHS) ester that reacts with the N-terminal amine or lysine residues of the peptide to form an amide bond. After rinsing in DMF, followed by ethanol, the tips are immersed in 0.2 mM peptide in phosphate buffered saline (PBS) overnight. Functionalized tips are rinsed in pure water prior to use.

If this approach is used to understand the role of protein-surface interactions in controlling the phenomenon of biomineralization, the most obvious configuration has the tip functionalized with the protein or a peptide fragment of that protein and the functionalized tip is interacted with a mineral surface. For a peptide chain, with presumably a single linkage to the tip, one cannot enact any level of control over conformation. However, a natural consequence of the molecular scale of the

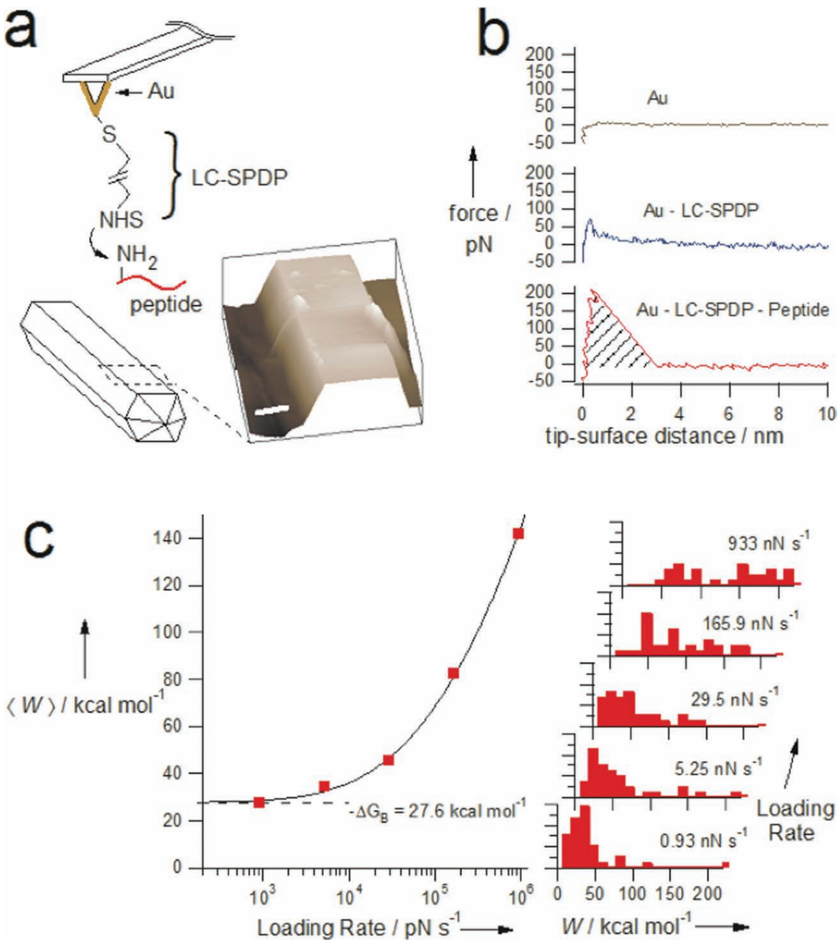

Figure 12. Determination of free energy of binding of the C-terminal sequence of amelogenin adsorbed to the (100) Face of HAP. a) The experimental set up involves linking the peptide to a gold-coated AFM cantilever by way of a bi-functional linker. The tip is placed directly on the (100) face of individual HAP crystals which were visible under bright field optics. The inset shows a typical AFM scan of an HAP crystal used to characterize the surface before force measurements (scale bar 4 µm). b) Representative force-distance curves for each level of functionalization (Au coating, LC-SPDP linker, and peptide) at approximately equivalent loading rates (4.7, 3.6, and 5.3 nN s^{-1} repectively). The hatched region indicates the work, *W*, measured upon moving the cantilever tip from the surface to the minimum of the pulling potential. c) Means (solid squares) and corresponding histograms (solid bars) of work measured from repeated force-distance trajectories for a peptide-functionalized tip (spring constant 93 pN nm^{-1}) from the (100) face of HAP. Solid curve is a fit to a two-state theoretical model given in the online Supporting Information of ref. [53] The mean work tends asymptotically to a finite value given by the free energy difference (dashed line) of $\Delta G_B = -27.6$ kcal mol^{-1}. The normalized histograms for increasing loading rate (0.93, 5.25, 29.5, 165.9, and 933 nN s^{-1}) are offset for clarity using identical ranges along the two axes. Reproduced with permission.[53]

system is that the peptide conformation fluctuates in between each force measurement simply due to Brownian motion, the same phenomenon responsible for ensuring that the data follow the predicted trend with loading rate. The dead time between each approach/retract cycle of force measurements is typically between about 1 to 20 s, depending on retraction speed. This includes the time the tip was pulled off the surface, retracted to the starting position, and then moved back to the surface to make contact for another measurement. This time span in which the peptide was out of contact with the crystal surface was long compared to the timescale of peptide conformational fluctuations, or even full conformational relaxation, which is often reported to be between nano- to milli-seconds. Thus averaging the work of adhesion over 40–100 repeated measurements at each site, provided an average over all of the explored conformations. In addition, a custom routine was used to randomly walk the AFM tip around the crystal surface between force measurements to account for surface inhomogeneities. Therefore the measurements approximated the ensemble average adhesion energy over peptide conformations that are accessible while linked to the tip, as well as over the various adhesion sites and geometries of the crystal.

Friddle et al.[53] used this approach to investigate the binding of the protein amelogenin to surfaces of single crystal calcium phosphate in the form of hydroxyapatite. This interaction is significant because amelogenin comprises the organic matrix that serves as a sacrificial scaffold for the formation of tooth enamel, which in turn is composed of a carbonated hydroxyapatite and is the hardest material in the human body.[54] To carry out the measurements, the rupture force between (100) faces of HAP crystals and tips functionalized with the 13-mer c-terminal peptide of amelogenin, which is believed to be the segment of the protein that binds to and modifies HAP growth,[55] (**Figure** 12A) were obtained under a calcium phosphate solution at approximately equilibrium saturation with respect to the HAP crystal. To account for any surface heterogeneity, a custom routine was used to randomly sample points on the surface to give a representative average. A constant approach velocity of 200 nm s^{-1} was used for every pulling velocity studied. A 2–3 nm deflection trigger was used to contact the surface and dwell for 1 second before pulling away.

Figure 12B shows representative force-distance trajectories for each level of chemical functionalization. Between 40 and 100 individual force-distance curves were collected and analyzed for pulling rate. The force-distance curves can be converted directly into the work *W* associated with breaking the Amel-HAP bond by integrating over the shaded area in Figure 12B. Because the bond rupture process is time-dependent, this work is greater than the equilibrium free energy of binding ΔG_B by an amount of dissipated heat, which decreases with decreasing loading rate dF/dt. As dF/dt approaches zero, the rate of bond breaking approaches its equilibrium value and the work done on the system should approach ΔG_B. Figure 12C shows the mean work <W> vs.

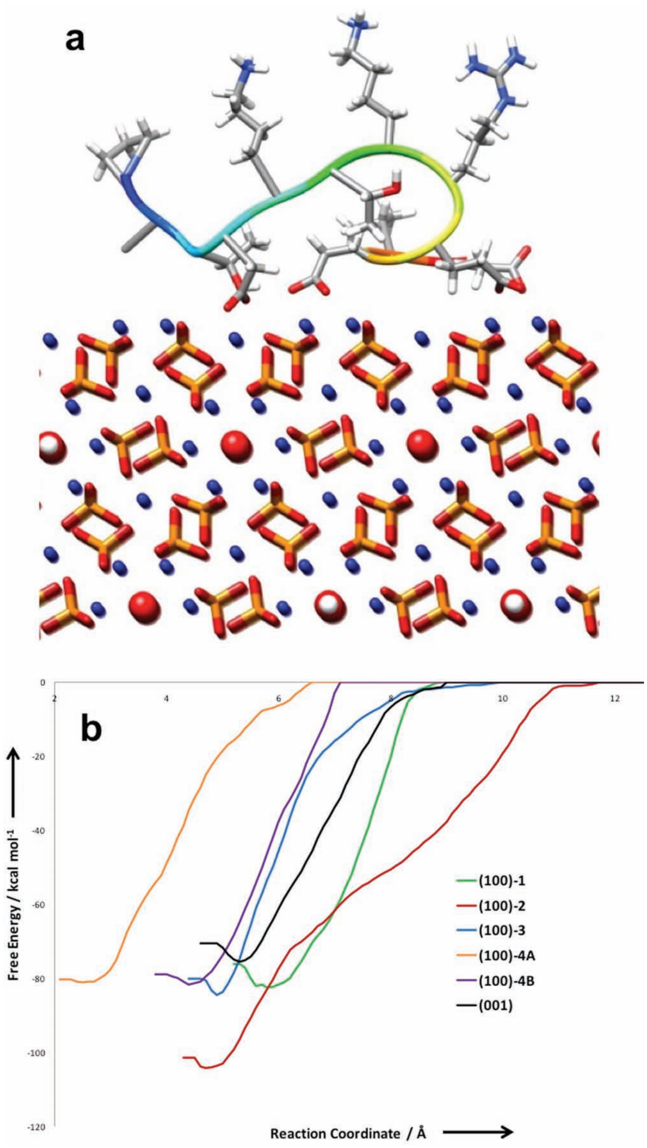

Figure 13. a) Initial Orientations of the 12-mer on the Calcium-terminated (100)-1 HAP surface. Calcium ions are depicted in blue (ball), hydroxide ions in red and white (CPK), and phosphates in red/orange (tube). The 12-mer backbone is depicted in rainbow as a tube, with blue representing the N-terminus (P-1) and red representing the C-terminus (D-12); selected nonpolar hydrogens are hidden from view. Five carboxylate moieties of the 12-mer account for the strong ionic attraction to the Ca^{2+}-terminated surfaces. Other (100) surface terminations 2, 3, 4A, and 4B, and an alternate (001) termination 2 are indicated. The hydroxides in the HAP lattice are emphasized as CPK to highlight the random orientations of the hydroxide columns. Insets: The solvated systems under periodic boundary conditions are shown, with water molecules represented as transparent isosurfaces. b) Adsorption free energy PMFs from ABF simulations for 12-mer/HAP Systems. Potentials are derived from several independent 500 ps simulations in which the center of the biasing potential of the 12-mer was "pulled" along the *z*-axis, normal to the HAP surfaces. The 12-mer binds more favorably to the various terminations of the (100) surface than to the (001) surfaces. Solid lines: (100)-1 (green), (100)-2 (red), (100)-3 (blue), (100)-4A (gold), (100)-4B (purple). Dashed line: (001)-1 (black); dot-dashed line: (001)-2 (black). Reproduced with permission.[53]

dF/dt and the corresponding normalized frequency histograms for each loading rate. As expected, <W> falls with decreasing loading rate and extrapolates to a finite value at $dF/dt = 0$. The solid curve in Figure 12C is a fit to the data according to the model of Friddle et al.[53] used in Figure 11. The fit to the data is excellent, and the asymptote gives $\Delta G_B = -27.6 \pm 1.5$ kcal mol^{-1}. Data for a second peptide-functionalized tip yielded $\Delta G_B = -29.5 \pm 1.3$ kcal mol^{-1}, giving an average value of $\langle \Delta G_B \rangle = -28.6 \pm 1.4$ kcal mol^{-1}.

The strong binding of this amelogenin peptide to the (100) face might provide an understanding of the extreme elongation of HAP crystals found in enamel as compared to geologic specimens.[56] However, this conclusion depends on knowledge of the relative binding strengths to these two faces. Unfortunately, the (001) face of the HAP crystals was too small to allow for physical mounting and alignment for a DFS measurement. Consequently, the result of the measurement on the (100) face was used to calibrate molecular dynamics (MD) calculations of amelogenin peptide binding to the HAP (100) face.[53] The MD analogue to a DFS experiment is called the potential of mean force (PMF). To obtain the PDF, the molecule is slowly pulled off and away from the surface and the required force is calculated (**Figure 13**). While DFS data could only be collected from the (100) face, PDF profiles could, of course, be obtained for any face. When the simulated value for the (100) face is calibrated using the experimentally determined value, the binding free energy to the (001) face is calculated to be lower by about 8.8 kcal mol^{-1}. Thus the results show that, indeed the binding free energy for the 12-residue amelogenin peptide to the (100) face far exceeds that to the (001) face and provides a possible rationale for the extreme aspect ratio observed tooth enamel.

5. Conclusion

The examples presented above demonstrate the deep level of understanding that can be obtained by applying in situ AFM imaging and force spectroscopy to biomolecular and biomineral systems. However, to date the processes and systems amenable to this method have been limited by two constraints. The first is speed. In conventional force microscopes, image collection times in non-contact mode are of order 10^2 s due to the low resonance frequency in water. In the past few years, we have seen the advent of high-speed AFM, for which scan speeds are 100–1000 times faster.[57] This capability will enable investigation of important processes in biomolecular and biomineral systems, such as conformational changes and protein folding events that occur too rapidly for conventional AFMs to resolve. Second, imaging of structures and processes on soft surfaces, such as cell membranes, has not been possible because the large amplitude of the cantilever's Brownian vibrations in fluid require use of large drive amplitudes in order to obtain a signal that is above the noise.[58] This large drive amplitude leads to unacceptable deformation of the material. For example, in the case of a cell membrane the deformation is so large that only the underlying cytoskeleton is resolved. New developments underway that remove the fluid-induced vibrations promise to deliver a molecular-scale view of these important and challenging systems.

Acknowledgements

This work was performed at the Molecular Foundry, Lawrence Berkeley National Laboratory, with support from the Office of Science, Office of Basic Energy Sciences, of the U.S. Department of Energy under Contract No. DE-AC02-05CH11231. Sandia is a multi-program laboratory operated by Sandia Corporation, a Lockheed Martin Company, for the United States Department of Energy under contract DE-AC04-94AL85000. The photograph for the inside cover was taken by R.W.F.

Received: November 21, 2012

[1] S. Mann, *Angew. Chem. Int. Ed.* **2008**, *47*, 5306.
[2] J. E. Johnson, *J. Struct. Biol.* **2008**, *163*, 246.
[3] R. N. Rambaran, L. C. Serpell, *Prion* **2008**, *2*, 112.
[4] C. Du, G. Falini, S. Fermani, C. Abbott, J. Moradian-Oldak, *Science* **2005**, *307*, 1450.
[5] S. Tanaka, C. A. Kerfeld, M. R. Sawaya, F. Cai, S. Heinhorst, G. C. Cannon, T. O. Yeates, *Science* **2008**, *319*, 1083.
[6] H. Engelhardt, *J. Struct. Biol.* **2007**, *160*, 115.
[7] S. Schultzelam, T. J. Beveridge, *Appl. Environ. Microb.* **1994**, *60*, 447.
[8] I. Cherny, E. Gazit, *Angew. Chem. Int. Ed.* **2008**, *47*, 4062.
[9] F. Chiti, C. M. Dobson, *Nat. Chem. Biol.* **2009**, *5*, 15.
[10] a) E. N. Salgado, R. A. Lewis, J. Faraone-Mennella, F. A. Tezcan, *J. Am. Chem. Soc.* **2008**, *130*, 6082; b) A. P. Schoen, D. T. Schoen, K. N. L. Huggins, M. A. Arunagirinathan, S. C. Heilshorn, *J. Am. Chem. Soc.* **2011**, *133*, 18202.
[11] M. D. Shoulders, R. T. Raines, *Annu. Rev. Biochem.* **2009**, *78*, 929.
[12] S. Chung, S. H. Shin, C. R. Bertozzi, J. J. De Yoreo, *Proc. Natl. Acad. Sci. USA* **2010**, *107*, 16536.
[13] S. H. Shin, S. Chung, B. Sanii, L. R. Comolli, C. R. Bertozzi, J. J. De Yoreo, *Proc. Natl. Acad. Sci. USA* **2012**, *109*, 12968.
[14] a) S. V. Albers, B. H. Meyer, *Nat. Rev. Microbiol.* **2011**, *9*, 414; b) U. B. Sleytr, P. Messner, D. Pum, M. Sara, *Angew. Chem. Int. Ed.* **1999**, *38*, 1035.
[15] M. Stewart, T. J. Beveridge, T. J. Trust, *J. Bacteriol.* **1986**, *166*, 120.
[16] a) W. Shenton, D. Pum, U. B. Sleytr, S. Mann, *Nature* **1997**, *389*, 585; b) D. Moll, C. Huber, B. Schlegel, D. Pum, U. B. Sleytr, M. Sara, *Proc. Natl. Acad. Sci. USA* **2002**, *99*, 14646.
[17] A. N. Naganathan, V. Munoz, *J. Am. Chem. Soc.* **2005**, *127*, 480.
[18] a) K. A. Dill, H. S. Chan, *Nat. Struct. Biol.* **1997**, *4*, 10; b) M. Gruebele, *Proc. Natl. Acad. Sci. USA* **2009**, *106*, 18879.
[19] S. E. Radford, *Trends Biochem. Sci.* **2000**, *25*, 611.
[20] Courtesy of Thomas Splettstoesser, www.scistyle.com (accessed October 2012).
[21] a) L. Addadi, S. Weiner, *Proc. Natl. Acad. Sci. USA* **1985**, *82*, 4110; b) S. Mann, *Nature* **1988**, *332*, 119.
[22] A. Berman, L. Addadi, S. Weiner, *Nature* **1988**, *331*, 546; G. Falini, S. Albeck, S. Weiner, L. Addadi, *Science* **1996**, *271*, 67.
[23] A. M. Belcher, X. H. Wu, R. J. Christensen, P. K. Hansma, G. D. Stucky, D. E. Morse, *Nature* **1996**, *381*, 56.
[24] a) S. Mann, J. M. Didymus, N. P. Sanderson, B. R. Heywood, E. J. A. Samper, *J. Chem. Soc. Faraday Trans* **1990**, *86*, 1873; b) A. P. Wheeler, K. C. Low, C. S. Sikes, *Surface Reactive Peptides and Polymers: discovery and commercialization*, ACS Books, Washington **1990**.
[25] a) L. Addadi, D. Joester, F. Nudelman, S. Weiner, *Chem. Eur. J.* **2006**, *12*, 981; b) L. Addadi, S. Raz, S. Weiner, *Adv. Mater.* **2003**, *15*, 959; c) L. B. Gower, D. J. Odom, *J. Cryst. Growth* **2000**, *210*, 719.
[26] Y. Politi, T. Arad, E. Klein, S. Weiner, L. Addadi, *Science* **2004**, *306*, 1161.
[27] J. H. Tao, D. M. Zhou, Z. S. Zhang, X. R. Xu, R. K. Tang, *Proc. Natl. Acad. Sci. USA* **2009**, *106*, 22096.
[28] R. M. H. Ravindranath, A. Devarajan, P. Bringas, *Arch. Oral. Biol.* **2007**, *52*, 1161.
[29] S. Weiner, L. Addadi, H. D. Wagner, *Mater. Sci. Eng. C* **2000**, *11*, 1.
[30] a) K. R. Cho, E. A. Salter, Y. Huang, A. Wierzbicki, J. J. De Yoreo, S. Elhadj, S. R. Qiu, *Cryst. Eng. Comm.* **2013**,*15*, 54; b) K. J. Davis, P. M. Dove, J. J. De Yoreo, *Science* **2000**, *290*, 1134; c) J. J. De Yoreo, P. M. Dove, *Science* **2004**, *306*, 1301; d) J. J. De Yoreo, S. R. Qiu, J. R. Hoyer, *Am. J. Physiol. Renal.* **2006**, *291*, F1123; e) S. Elhadj, E. A. Salter, A. Wierzbicki, J. J. De Yoreo, N. Han, P. M. Dove, *Cryst. Growth Des.* **2006**, *6*, 197; f) G. Fu, S. R. Qiu, C. A. Orme, D. E. Morse, J. J. De Yoreo, *Adv. Mater.* **2005**, *17*, 2678; g) S. W. Guo, M. D. Ward, J. A. Wesson, *Langmuir* **2002**, *18*, 4284; h) T. Jung, X. X. Sheng, C. K. Choi, W. S. Kim, J. A. Wesson, M. D. Ward, *Langmuir* **2004**, *20*, 8587; i) C. A. Orme, A. Noy, A. Wierzbicki, M. T. McBride, M. Grantham, H. H. Teng, P. M. Dove, J. J. DeYoreo, *Nature* **2001**, *411*, 775; j) H. H. Teng, P. M. Dove, C. A. Orme, J. J. De Yoreo, *Science* **1998**, *282*, 724.
[31] R. W. Friddle, M. L. Weaver, S. R. Qiu, A. Wierzbicki, W. H. Casey, J. J. De Yoreo, *Proc. Natl. Acad. Sci. USA* **2010**, *107*, 11.
[32] S. R. Qiu, A. Wierzbicki, C. A. Orme, A. M. Cody, J. R. Hoyer, G. H. Nancollas, S. Zepeda, J. J. De Yoreo, *Proc. Natl. Acad. Sci. USA* **2004**, *101*, 1811.
[33] S. R. Qiu, A. Wierzbicki, E. A. Salter, S. Zepeda, C. A. Orme, J. R. Hoyer, G. H. Nancollas, A. M. Cody, J. J. De Yoreo, *J. Am. Chem. Soc.* **2005**, *127*, 9036.
[34] M. L. Weaver, S. R. Qiu, R. W. Friddle, W. H. Casey, J. J. De Yoreo, *Cryst. Growth Des.* **2010**, *10*, 2954.
[35] M. L. Weaver, S. R. Qiu, J. R. Hoyer, W. H. Casey, G. H. Nancollas, J. J. De Yoreo, *J. Cryst. Growth* **2007**, *306*, 135.
[36] Y. Shirane, S. Kagawa, *J. Urol.* **1993**, *150*, 1980.
[37] J. J. De Yoreo, P. G. Vekilov, *Rev. Mineral Geochem.* **2003**, *54*, 57.
[38] P. A. Mulheran, D. Pellenc, R. A. Bennett, R. J. Green, M. Sperrin, *Phys. Rev. Lett.* **2008**, *100*, 068102.
[39] M. Bachmann, W. Janke, *Phys. Rev. Lett.* **2005**, *95*, 058102.
[40] a) J. R. Hoyer, J. R. Asplin, L. Otvos, *Kidney Int.* **2001**, *60*, 77; b) H. Shiraga, W. Min, W. J. Vandusen, M. D. Clayman, D. Miner, C. H. Terrell, J. R. Sherbotie, J. W. Foreman, C. Przysiecki, E. G. Neilson, J. R. Hoyer, *Proc. Natl. Acad. Sci. USA* **1992**, *89*, 426.
[41] J. H. Harding, D. M. Duffy, M. L. Sushko, P. M. Rodger, D. Quigley, J. A. Elliott, *Chem. Rev.* **2008**, *108*, 4823.
[42] J. J. De Yoreo, A. Wierzbicki, P. M. Dove, *Cryst. Eng. Comm.* **2007**, *9*, 1144.
[43] V. I. Armol'd, *Catastrophe Theory*, Springer, New York **1986**.
[44] E. Evans, *R. Soc. Chem., Faraday Discuss.* **1998**, *111*, 1.
[45] H. Eyring, *J. Chem. Phys.* **1936**, *4*, 283.
[46] R. Merkel, P. Nassoy, A. Leung, K. Ritchie, E. Evans, *Nature* **1999**, *397*, 50.
[47] A. Tobolsky, H. Eyring, *J. Chem. Phys.* **1943**, *11*, 125.
[48] S. N. Zhurkov, *Int. J. Fract. Mech.* **1965**, *1*, 311.
[49] G. I. Bell, *Science* **1978**, *200*, 618.
[50] E. Evans, K. Ritchie, *Biophys. J.* **1997**, *72*, 1541.
[51] E. Evans, *Physics of bio-molecules and cells. (Physique des biomolécules et des cellules)*, Springer, Berlin/Heidelberg **2002**.
[52] R. W. Friddle, A. Noy, J. J. De Yoreo, *Proc. Natl. Acad. Sci. USA* **2012**, *109*, 13573.
[53] R. W. Friddle, K. Battle, V. Trubetskoy, J. H. Tao, E. A. Salter, J. Moradian-Oldak, J. J. De Yoreo, A. Wierzbicki, *Angew. Chem. Int. Ed.* **2011**, *50*, 7541.
[54] a) H. C. Margolis, E. Beniash, C. E. Fowler, *J. Dent. Res.* **2006**, *85*, 775; b) C. Robinson, J. Kirkham, A. S. Hallsworth, *Arch. Oral. Biol.* **1988**, *33*, 159.
[55] J. Moradian-Oldak, J. Tan, A. G. Fincham, *Biopolymers* **1998**, *46*, 225.
[56] a) R. J. Radlanski, W. Seidl, G. Steding, A. Jager, *Anat. Anz.* **1989**, *168*, 405; b) S. Weiner, H. D. Wagner, *Annu. Rev. Mater. Sci.* **1998**, *28*, 271.
[57] N. Kodera, D. Yamamoto, R. Ishikawa, T. Ando, *Nature* **2010**, *468*, 72.
[58] B. Sanii, P. D. Ashby, *Phys. Rev. Lett.* **2010**, *104*, 147203.